INTERNATIONAL JOURNAL FOR NUMERICAL METHODS IN FLUIDS
Int. J. Numer. Meth. Fluids 2000; **32**: 1021–1047

Numerical modelling and validation of Marangoni and surface tension phenomena using the finite volume method

D. Wheeler, C. Bailey* and M. Cross

Centre for Numerical Modelling and Process Analysis, University of Greenwich, Wellington Street, London, U.K.

SUMMARY

Surface tension induced flow is implemented into a numerical modelling framework and validated for a number of test cases. Finite volume unstructured mesh techniques are used to discretize the mass, momentum and energy conservation equations in three dimensions. An explicit approach is used to include the effect of surface tension forces on the flow profile and final shape of a liquid domain. Validation of this approach is made against both analytical and experimental data. Finally, the method is used to model the wetting balance test for solder alloy material, where model predictions are used to gain a greater insight into this process. Copyright © 2000 John Wiley & Sons, Ltd.

KEY WORDS: Marangoni flow; numerical modelling; surface tension

1. INTRODUCTION

Investigations of thermo-capillary flows with a deforming free surface have been performed using a number of discretization techniques, such as the spectral method [1], finite volume method (FVM) [2] and the finite element method (FEM) [3,4]. Each approach aims to include surface tension forces within a numerical fluid framework to accurately predict the effect of surface tension on the flow field and the position of the free surface.

Using the spectral method in two dimensions, Ahmed *et al.* [1] investigated both Marangoni and buoyancy driven flow for low capillary numbers (Ca). Periodically during the simulation, the free surface is updated using the normal stress approach, and the mesh is regenerated using body-fitted co-ordinates. Although comparisons with literature data are encouraging, it should be noted that extensions to three dimensions using a spectral method, with mesh regeneration at each free surface update, will be computationally expensive.

* Correspondence to: School of Computing and Mathematical Sciences, The University of Greenwich, Woolwich University Campus, Wellington Street, Woolwich, London SE18 6PF, U.K.

Received November 1998
Revised July 1999

Sasmal *et al.* [2] adopted the FVM to discretize the Navier–Stokes and temperature equations in two dimensions. In this approach, a Cartesian mesh was used and the deforming free surface is modelled using the volume-of-fluid (VOF) algorithm. The attraction of this approach is that mesh movement is avoided, but surface smearing may result owing to numerical diffusion.

McClelland [3] used the FEM to discretize the Navier–Stokes and temperature equations in two dimensions. The free surface is modelled using a kinematic update, where the calculated surface velocity is used to update its position. The surface tension boundary condition is integrated by parts to avoid computation of curvature. Good results were obtained, but spurious oscillations were encountered owing to the explicit nature of the surface tension source terms.

Slikkerveer *et al.* [4] solved for Stokes flow in two dimensions using the FEM. A compact solver was used to solve the flow variables simultaneously. To overcome the observed numerical instability with regard to the kinematic mesh update, an implicit scheme was adopted. An important issue raised in this paper, regarding the instability of the free surface, is the time step required for the kinematic update, which has to be an order smaller then the minimum time scale for the system. The time scale depends on the square of the wavelength of the free surface. The wavelength in the numerical problem depends on the mesh size. Thus, the time step size has to be decreased, as the mesh is refined.

Marangoni and surface phenomena provide an interesting area for investigation both from the academic and the industrial viewpoints. One industrial application that is governed by this phenomenon lies in the area of electronic packaging, where solder material melts, reflows and then solidifies to bond electronic components to printed circuit boards (PCBs). The effect of surface tension on solder joint formation has received a large amount of attention, specifically in the initial shape predication of solder joints [5], which have been modelled numerically using the SURFACE EVOLVER (SE) package [6,7]. These shape predictions have been coupled with computational mechanics codes to further predict solidification [8] and then residual stress [8,9] within the solder and its surroundings. In this paper, simulations involving the wetting balance test are undertaken. The wetting balance test is used to establish the wettability of electronic component surfaces [10]. Experimental investigations on this test have shown that the change in solder height is not fully explained by the elastica solution.

In this paper, the geometry is updated at the end of each time step stage with a relaxation method to improve the stability at the free surface. This paper contributes to the modelling of surface tension dominated process by

- representing of the governing conservation equations, including surface tension in a three-dimensional finite volume framework;
- discretization of the surface tension boundary condition as a line integral as opposed to a surface integral;
- investigation into stability of the free surface.

This method is validated against both analytical solutions and used to gain an insight into forces acting in the wetting balance test.

2. GOVERNING EQUATIONS

The governing equations described here as the momentum and mass conservation equations in three dimensions with heat transfer. Also described is the surface tension boundary condition deriving the weak form, from the strong form using finite volume methodology. Generally, between two different fluids there exists a film that may have a surface tension associated with it that can be represented as normal and tangential forces. Typically, one of the fluids will have a negligible effect on the film. A tangential force will be present if the surface tension differs along the free surface. This is the force that acts as a boundary condition to induce Marangoni flow. The surface tension difference along an interface may be caused by a number of factors including temperature or concentration gradients. The surface tension, γ_i, may be a function of these quantities, such that

$$\gamma = \gamma(T(\underline{r}), S_i(\underline{r})) \tag{1}$$

where $T(\underline{r})$ is temperature as a function of position $\underline{r}$, and $S_i(\underline{r})$ is a proportion of a chemical species. A normal force will be present wherever surface tension exists unless the curvature of the surface vanishes.

2.1. Mass conservation

The equation for mass conservation, using tensor notation, is

$$\int_V \frac{\partial \rho}{\partial t}\, \mathrm{d}V + \int_{\partial V} n_i u_i \rho\, \mathrm{d}(\partial V) = 0, \quad i = x, y, z \tag{2}$$

where V is an arbitrary volume, ρ is the density, t is the time, u_i is the velocity and n_i is the normal to the free surface, and ∂V is the surface of the volume.

2.2. Momentum conservation

The governing equation for conservation of momentum is

$$\int_V \frac{\partial}{\partial t}(\rho u_i)\, \mathrm{d}V + \int_{\partial V} n_j u_j \rho u_i\, \mathrm{d}(\partial V) = \int_{\partial V} \sigma_{ij} n_j\, \mathrm{d}(\partial V) + S_{u_i}, \quad i = x, y, z \tag{3}$$

where S_{u_i} are the source terms and σ_{ij} is the fluid stress tensor.

2.3. Enthalpy conversation

The equation of enthalpy conservation [11–13] for an incompressible low-velocity flow with negligible viscous dissipation is

$$\int_V \frac{\partial}{\partial t}(\rho h)\, \mathrm{d}V + \int_{\partial V} n_i u_i \rho h\, \mathrm{d}(\partial V) = \int_{\partial V} n_i k \frac{\partial}{\partial x_i} T\, \mathrm{d}(\partial V) + S_h \tag{4}$$

where h is the reduced enthalpy, c is the specific heat and k is the thermal conductivity. The reduced enthalpy is related to temperature, T, via

$$h = cT \tag{5}$$

2.4. Surface tension boundary condition

The surface tension boundary condition is presented in three dimensions for a thin film between two fluids where one of the fluids has negligible influence [14], such that

$$n_i \sigma_{ij} n_j = -p_a + J\gamma \tag{6}$$

$$t_i \sigma_{ij} n_j = t_j \frac{\partial \gamma}{\partial x_j} \tag{7}$$

and

$$m_i \sigma_{ij} n_j = m_j \frac{\partial \gamma}{\partial x_j} \tag{8}$$

The vectors t_i and $m_i = \varepsilon_{ijk} n_k t_j$ are unit tangents to the surface, J is the first curvature of the surface and p_a is the external pressure. Equation (6) is the normal boundary condition and Equations (7) and (8) are the tangential boundary conditions. An alternative representation [15] is

$$\sigma_{ij} n_j = J\gamma n_i - p_a n_i + (\delta_{ij} - n_i n_j) \frac{\partial \gamma}{\partial x_j}, \quad i = x, y, z \tag{9}$$

Equations (6)–(8) can be seen by dot multiplying Equation (9) by n_i, t_i and m_i respectively. Equations (6)–(9) are the strong forms of the boundary condition. It is necessary, for the FVM, to derive the weak form of the boundary condition. The following result is useful for this derivation:

$$\int_S \nabla_S \phi \, \mathrm{d}S = \oint_{\partial S} \underline{m} \phi \, \mathrm{d}(\partial S) - \int_S J \phi \underline{n} \, \mathrm{d}S \tag{10}$$

where

$$\nabla_{S_i} = (\delta_{ij} - n_i n_j) \frac{\partial}{\partial x_j} \tag{11}$$

The vector m_i is the unit tangent to the surface, but normal to the boundary enclosing the surface. Equation (10) is the divergence theorem on a curved surface, for a function ϕ defined on the surface S, differing from the result for a flat surface due to the extra curvature integral,

Weatherburn [16], p. 240. To derive the weak form of the boundary condition, Equation (9) is integrated over a portion of the surface to give

$$\int_S \sigma_{ij} n_j \, \mathrm{d}S = \int_S J\gamma n_i \, \mathrm{d}S - \int_S p_a n_i \, \mathrm{d}S + \int_S (\delta_{ij} - n_i n_j) \frac{\partial \gamma}{\partial x_j} \, \mathrm{d}S \tag{12}$$

By applying the divergence theorem given in Equation (10) to the last term in Equation (12), the curvature cancels to leave

$$\int_S \sigma_{ij} n_j \, \mathrm{d}S = -\int_S p_a n_i \, \mathrm{d}S + \oint_{\partial S} m_i \gamma \, \mathrm{d}(\partial S) \tag{13}$$

Equation (13) is a useful representation for the FVM. The last term in Equation (13) can be seen from first principles since it is just the magnitude and direction of the force due to surface tension summed around the edge of the surface S. The general finite element equivalent employing a test function ϕ is [4]

$$\int_S \sigma_{ij} n_j \phi \, \mathrm{d}S = -\int_S p_a n_i \phi \, \mathrm{d}S - \int_S \gamma (\delta_{ij} - n_i n_j) \frac{\partial \phi}{\partial x_j} \, \mathrm{d}S + \oint_{\partial S} \phi m_i \gamma \, \mathrm{d}(\partial S) \tag{14}$$

Implementation of Equation (13) into the discretized momentum equation in a computational fluid dynamics (CFD) framework is simpler than that of Equation (4) owing to the removal of the second term on the right-hand side of Equation (14). Thus, the requirement of computing an extra term over a piecewise surface is overcome by using the FVM, although a tangent vector m_i must still be interpolated between adjacent facets on the free surface.

3. MODELLING FRAMEWORK

PHYSICA [17] is a numerical framework for the modelling of physical phenomena where materials may exhibit solid and/or fluid behaviour during their processing. A range of interacting solution procedures for turbulent flow, heat transfer with solidification/melting and elasto-visco-plastic solid mechanics are included. This code has been used extensively to model a number of industrial processes [18,19]. A cell-centred FVM [20] using the SIMPLE [12] procedure is employed to solve the mass, momentum and energy equations [where the control volume (CV) corresponds to the mesh element]. Dependent variables such as temperature, pressure and velocity components are stored at the centre of the CV. Pressure–velocity decoupling is avoided by the use of Rhie–Chow interpolation. For a free surface a constant pressure boundary condition is used. The solution procedure for the mass and momentum equation is outlined below.

1. Guess an initial pressure and velocity field.
2. Solve for new velocities using the discretized momentum equation.
3. Solve the pressure correction equation.

4. Calculate the velocity corrections using the pressure corrections.
5. Update the velocity and pressure fields using the corresponding corrections.
6. If convergence criteria not satisfied, return to 2 using new velocity and pressure field as the guessed values.

A complete solution procedure can be seen in Figure 3. In this analysis, the Laplace equation is used to adjust the mesh where the CVs are built up around the vertices. This is the vertex based [21] approach to the FVM, where dependent variables such as displacements are located at mesh vertices as illustrated in Figure 1.

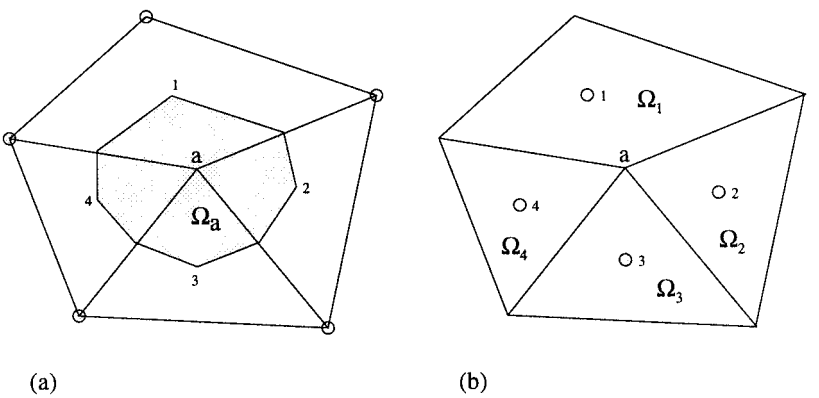

Figure 1. FVM for an unstructured mesh: (a) vertex-based, (b) cell-centred; Ω represents a CV.

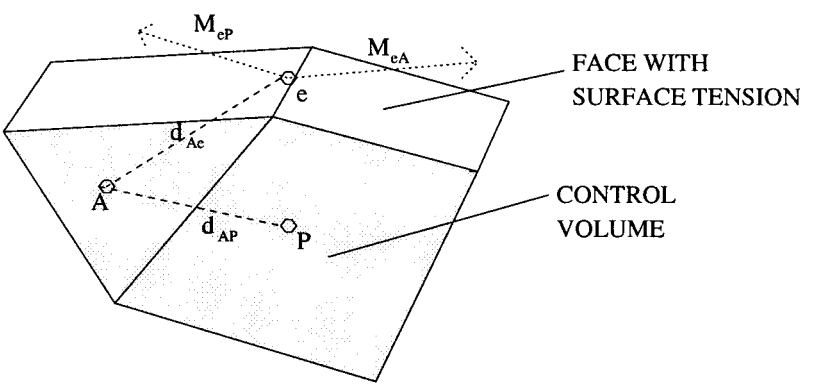

Figure 2. CV diagram.

3.1. Discretization

The right-hand side of Equation (13) must be approximated around the boundary of each element face that has surface tension. This produces a source term for the momentum equations on elements that are adjacent to the free surface. Surface tension is evaluated at every edge, using a linear interpolation for temperature between two neighbouring cell centres as illustrated in Figure 2. Equation (13) is discretized as follows:

$$-\int_S p_a n_i \, \mathrm{d}S + \oint_{\partial S} m_i \gamma \, \mathrm{d}(\partial S) = -p_a (n_i A)_f + \sum_e (m_i \gamma l)_e \tag{15}$$

where the summation is over all the edges e of the surface of an element, which lies adjacent to the interface; the length of the edge is l_e, and A_f is the area of the face. The surface tension at an edge is evaluated via $\gamma_e = \gamma(T_e)$. The temperature at the edge T_e is approximated using

$$T_e = \alpha_e T_P + (1 - \alpha_e) T_A \tag{16}$$

where

$$\alpha_e = \frac{d_{Ae}}{d_{Ae} + d_{eP}} \tag{17}$$

d_{Ae} is the distance from the adjacent element centre to the edge centre. The temperature in an element E is represented by T_E. The tangent m_{ie} at the edge between two faces must be approximated and to ensure conservation, the value of m_{ie} due to one face must be equal and opposite on any adjacent surface face, therefore

$$m_{ie} p = \varepsilon_{ijk} n_{iP} t_{jeP} \tag{18}$$

where t_{jeP} is the tangent vector to the face of the element associated with the edge (i.e. it is the unit vector along the edge in the direction due to the right hand rule) and n_{ip} is the normal of the face pointing out of the element. So m_{ie} can be expressed by

$$m_{ie} = \frac{m_{ieP} - m_{ieA}}{2} \tag{19}$$

During the solution procedure, the fluid motion due to Marangoni and buoyancy forces updates the boundary of the domain using a mixed Lagrangian approximation. The velocity at the surface nodes that are calculated from the face fluxes is then used to update the free surface position. Internal nodes are then moved to keep a satisfactory mesh definition, which must be reflected in the transient and convection terms of the general equation to preserve the dependent variable [22]. The discretization of the continuity equation (2) must include volume changes in the control volume where

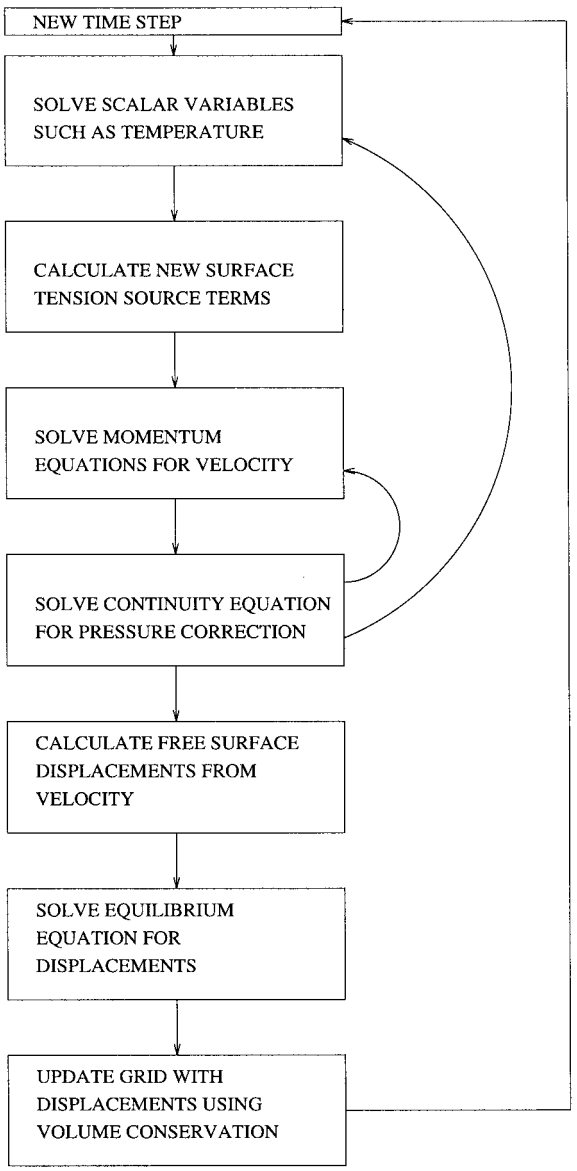

Figure 3. Solution procedure.

$$\int_{t-\Delta t}^{t}\int_{V}\frac{\partial\rho}{\partial t}\,\mathrm{d}V\,\mathrm{d}t+\int_{t-\Delta t}^{t}\int_{\partial V}n_i u_i\rho\;\mathrm{d}(\partial V)\,\mathrm{d}t=0 \tag{20}$$

and discretized in the following manner:

$$V_P\rho_P-V_P^0\rho_P^0+\sum_f\rho_f((u_i-u_{iM})n_i)_f A_f\Delta t=0 \tag{21}$$

where Δt is the time step size, V_P is the volume of the element, V_P^0 is the volume of the element at the previous time step, and u_{iM} is the mesh velocity. For the case of constant density, Equation (21) becomes

$$\sum_f(u_i n_i)_f A_f=0 \tag{22}$$

If the momentum equation (3) above is integrated in a similar manner to Equation (20), the discretization of the left-hand side is

$$V_P\rho_P u_{iP}-V_P^0\rho_P^0 u_{iP}^0+\sum_f\rho_f((u_j-u_{jM})n_j)_f A_f u_{if}\Delta t \tag{23}$$

3.2. Dynamic mesh deformation

The mesh face velocity is calculated via

$$u_{iM}=\frac{r_i-r_i^0}{\Delta t} \tag{24}$$

where r_i is the current face centre and $r_i^o$is the old face centre. u_{iM} must be updated after each time step. The surface grid velocity is required and is calculated via

$$u_{iG}=\frac{\sum_f u_i f}{n_f} \tag{25}$$

where u_{iG} is evaluated over all adjacent free surface faces, n_f is the number and u_{if} is the velocity normal to each of these faces. The velocities u_{if} are calculated from the face fluxes such that

$$u_{if}=\frac{F_f n_i}{\rho_f A_f} \tag{26}$$

where F_f is the face flux. The surface grid velocities, located at mesh vertices, are calculated at each time step. These values can be used as displacement boundary conditions $\delta x_{iG}=u_{iG}\Delta t$ to deform the mesh. An equilibrium calculation [21,22] is used to deform the internal governed by the following equation:

$$\frac{\partial^2 d_i}{\partial x_i \partial x_j} = 0 \tag{27}$$

where d_i is the displacement field with

$$d_i = \delta x_i \tag{28}$$

at the boundary. Equations (27) and (28) are discretized using the vertex based FVM. The internal nodes are displaced avoiding any change in topology using the solution procedure in Figure 3. Relaxation of the mesh movement was included on the surface by using the previous time step displacement, which prevents instabilities that can occur owing to using a first-order scheme in time for Equation (15). The surface displacement with the relaxation can be written

$$\delta x = (1 - \alpha)\delta x_G + \alpha \delta x_0 \tag{29}$$

where δ_{x0} is δx evaluated at the previous time step and α is the relaxation value.

4. NUMERICAL EXAMPLES

The algorithms described above are validated against four separate test cases. The first two test cases are closed form solutions derived using lubrication theory to approximate the steady incompressible flow field at small Marangoni numbers. However, the numerical solution is not restricted to small Marangoni number. The last two test cases model the wetting balance test in both two and three dimensions [10]. The aims of the validation cases are

- Case 1: validate Marangoni flow with a fixed flat free surface due to a temperature gradient.
- Case 2: validate Marangoni flow for a fixed curved surface and investigate the effects of temperature interpolation from the cell centres.
- Case 3: validate static free surface position and the effect of Marangoni flow. Investigate the effect of buoyancy and combined buoyancy–Marangoni flow.
- Case 4: validate static free surface position in three dimensions. Investigate the effect of Marangoni flow.

4.1. Case 1: thermo-capillary motion of a liquid with a free surface, with non-linear dependence of the surface tension on the temperature

In this example [23], the surface tension γ has a quadratic dependence on temperature,

$$\gamma = \gamma_0 + \frac{1}{2}\alpha(T - T_0)^2 \tag{30}$$

on the upper surface of the domain, while the bottom surface has a surface temperature boundary condition $T = T_0 + Ax$, where A is a constant. The similarity solution can be found for small Marangoni number, defined by

$$M_h = \frac{\rho H^3 \alpha A^2}{\mu^2} \tag{31}$$

where μ is viscosity and H is the height of the cavity. All the constants in Equation (31) were set at unity apart from H. Three meshes are used to model this problem using 700 (7×100), 1650 (11×150), and 3000 (15×200) elements. The 3000 elements mesh can be seen in Figure 4 and the velocity vectors are plotted in Figure 5. The length of the rectangular cavity was set at 10 and the height $H = 0.4$. Figures 6–8 show the percentage difference between the numerical and the analytical solutions, illustrated in Figure 9 for different mesh densities. The plots show that all mesh densities come within a 10 per cent difference of the closed form solution, the first mesh is within a 2 per cent difference and as the mesh is refined the difference decreases. The given closed form solution is for a domain of infinite extent. The numerical domain had to be of a finite extent so the limit of $x = 10$ was chosen, which simulates an infinite extent for the region away from $x = 10$. In Figure 6, the error is seen to increase at $x = 10$; this is due to the numerical solution not modelling the closed form solution at this point. This does not effect the solution in the region of concern near $x = 0$. These results validate the above finite volume framework, where surface tension effects are included and the interface remains flat.

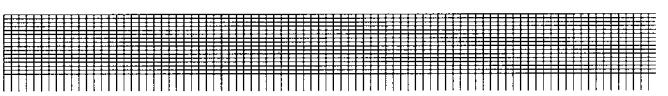

Figure 4. The 3000 element mesh used for the simulation.

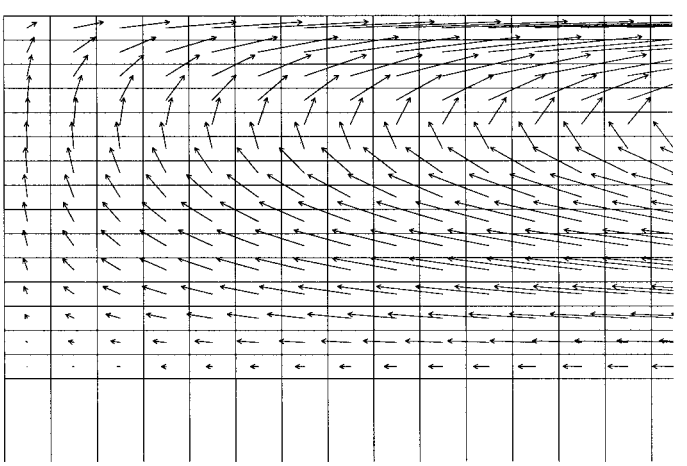

Figure 5. The velocity vectors for the 3000 element mesh

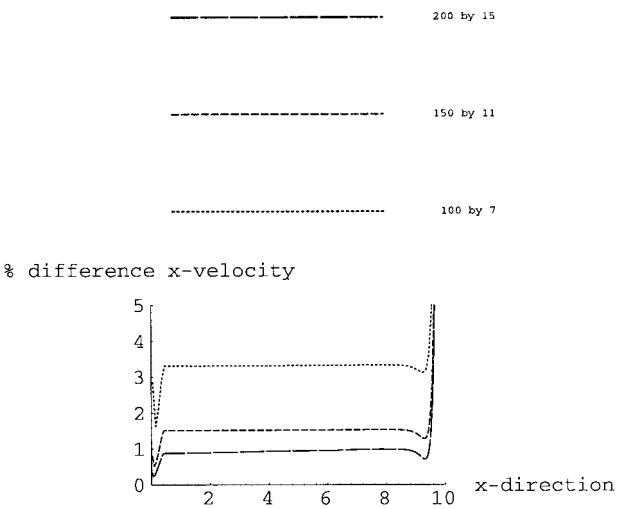

Figure 6. Per cent difference for the x velocity in the x-direction at $y = 0.387$.

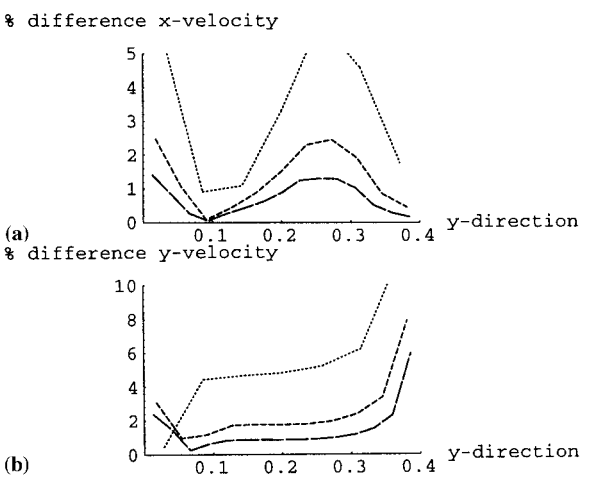

Figure 7. Per cent difference for (a) x velocity and (b) y velocity in the y-direction at $x = 0.257$.

4.2. Case 2: non-isothermal spreading of liquid drops on horizontal plates

Erhard and Davis [24] found closed form solutions for a two-dimensional liquid drop when the free surface had reached equilibrium at small Marangoni number M_c, and small contact angle θ. The surface tension was allowed to vary linearly with temperature and is given by

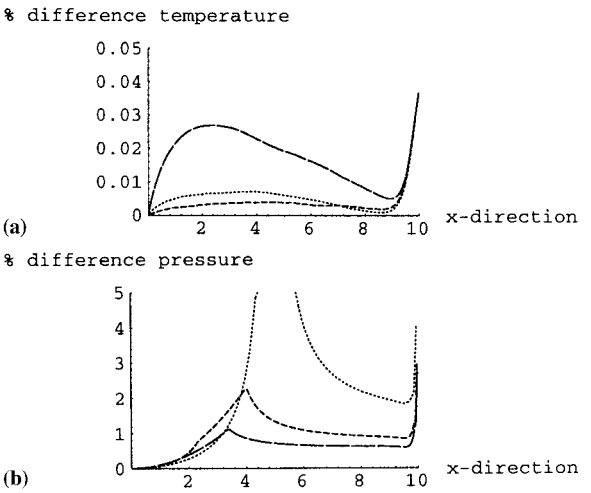

Figure 8. Per cent difference for (a) temperature and (b) pressure in the x-direction at $y = 0.2$.

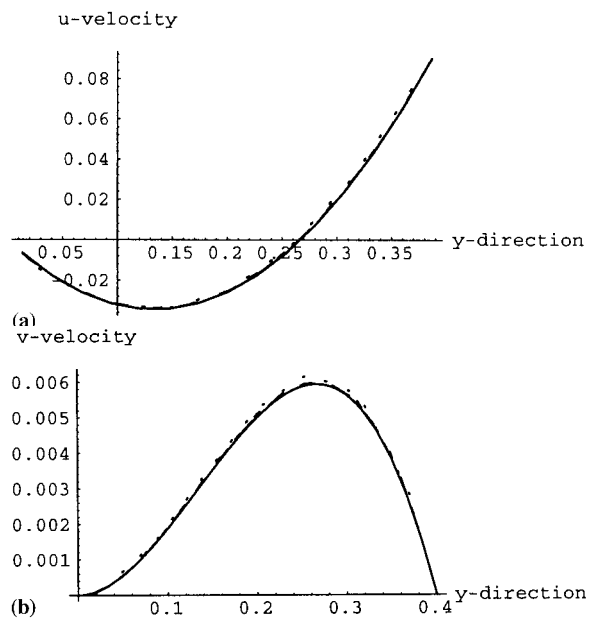

Figure 9. The (a) x velocity and (b) y velocity in the y direction at $x = 0.257$.

Figure 10. 180×9 element mesh used for the simulation.

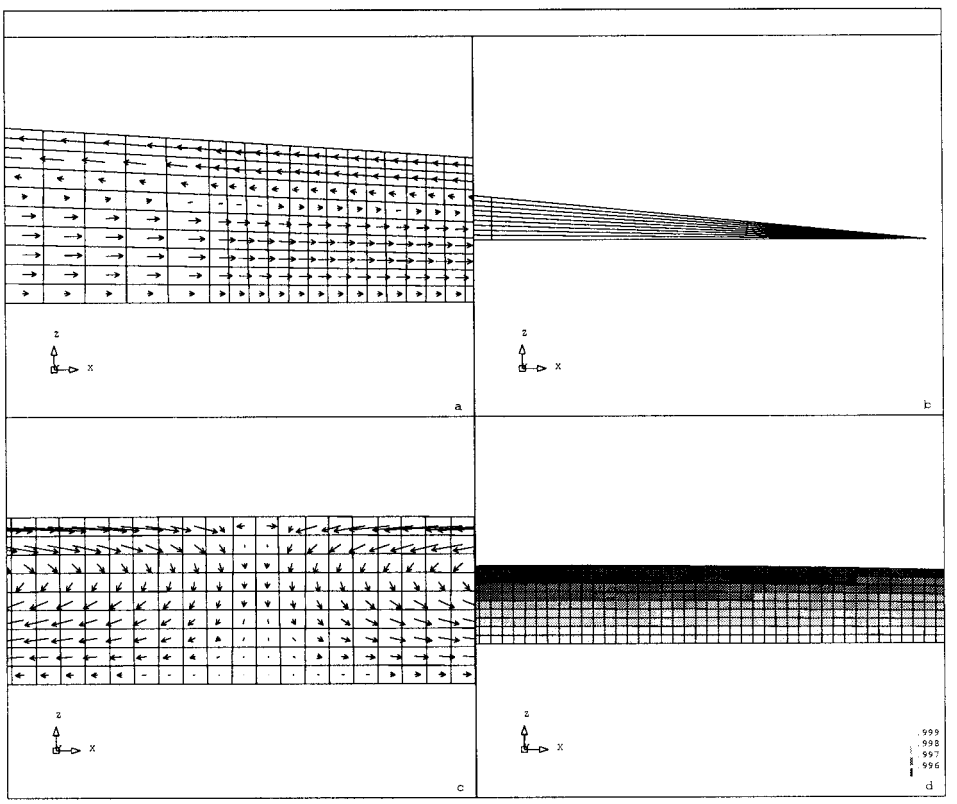

Figure 11. Sections for the 180×9 element mesh of (a) velocity vectors at $x = 0.66$ showing the region where the mesh aspect ratio doubles; (b) small aspect ratio elements near the corner of the mesh, which lead to inaccuracies in this region; (c) velocity vectors at $x = 0$, where the solution is the most accurate; (d) temperature in cavity.

$$\gamma = \gamma_w - \gamma_0(T - T_w) \tag{32}$$

where T_w is the fixed temperature along the bottom surface. In this simualtion, $\theta = 0.1$ and $M_c = 0.01$. Again a number of mesh densities were used, 180×9, 140×4, 100×5 and 60×3 elements. The largest mesh can be seen in Figures 10 and 11. The velocity vectors are illustrated in Figure 11(a) and (c). Figure 11(d) shows the temperature in a section of the drop.

In this test case, the free surface position is calculated from the analytical solution and imposed on the mesh. A further case was studied using the analytical temperature field, eradicating any spurious errors owing to temperature extrapolation from the cell centres to the nodes. Figures 12–15 show plots of the per cent difference between the analytical and numerical results. For the finest mesh, the difference is less than 10 per cent for each variable. In each plot there is (a) a clear loss of accuracy owing to the temperature extrapolation from the cell centres to the free surface nodal points, and (b) an improvement in accuracy as the mesh is refined in all cases. In Figure 12 there is a spike in the region where the mesh experiences a sudden refinement at $x = \frac{2}{3}$. The tangential temperature extrapolation becomes inaccurate at this point because the grid node no longer lies equi-distance between the cell centres. This is confirmed by the use of the prescribed temperature, which eradicates the spike. In Figures 13 and 14(a)

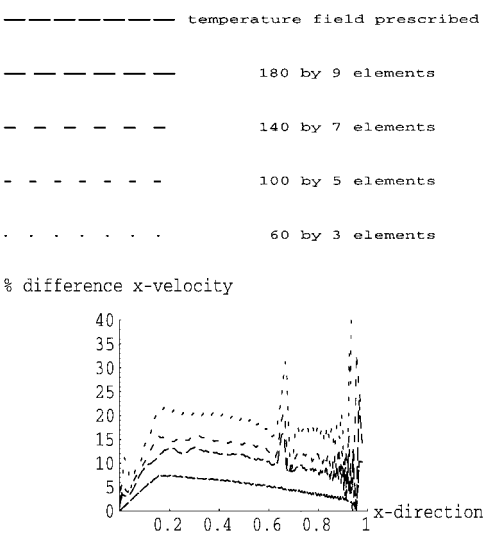

Figure 12. Per cent difference for the x velocity in the x-direction for $z = 8.5h/9$.

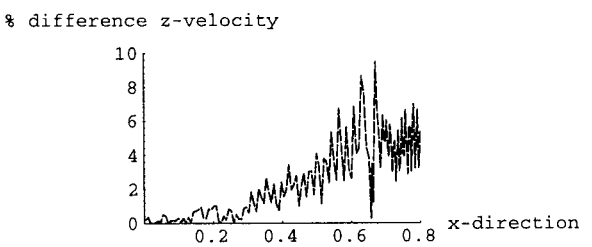

Figure 13. Per cent difference for the z velocity in the x-direction for $z = h/2$.

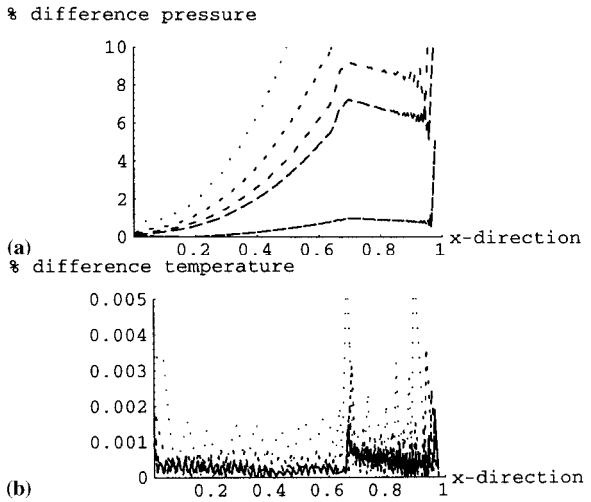

Figure 14. Per cent difference for (a) pressure and (b) temperature in the x-direction at $z = h/2$.

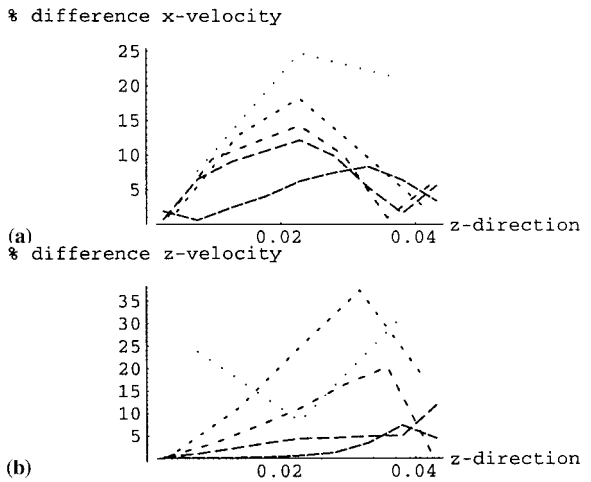

Figure 15. Pre cent difference for (a) x velocity and (b) z velocity in the z-direction at $x = 0.1$.

there is a loss of accuracy due to the small height in this region leading to large aspect ratio elements, which can be seen in Figure 11(b). All the meshes used here were coarse but sufficient to indicate a convergence to the analytical result. These results validate the algorithm for an interface that has changing curvature.

4.3. Case 3: simulation of the wetting balance test in two dimensions

The simulation was attempted to identify the dominant force effecting, and to accurately predict, meniscus height rise in the wetting balance test building on earlier experimental work by Moon *et al.* [10]. The experimental work examined oil and solder at different temperatures, measuring the force, angle and height rise at the contact triple point in each case. The height measured in the experiment could not be accounted for by standard static equilibrium theory. It was conjectured that resultant steady state flow may be occurring due to temperature variations in the fluid, which may affect the equilibrium free surface position. The problem was modelled in two dimensions with the solder bath domain represented by a $1 \times 0.5\,\mathrm{cm}^2$ rectangle, and a contact angle of 45° at the triple point, as shown in Figure 16. The material properties for oil and solider are listed in Table I.

The physical system can be characterized by various dimensionless parameters, beginning with the static bond number given by

$$B_0 = \frac{\rho_0 g H^2}{\gamma_0} \tag{33}$$

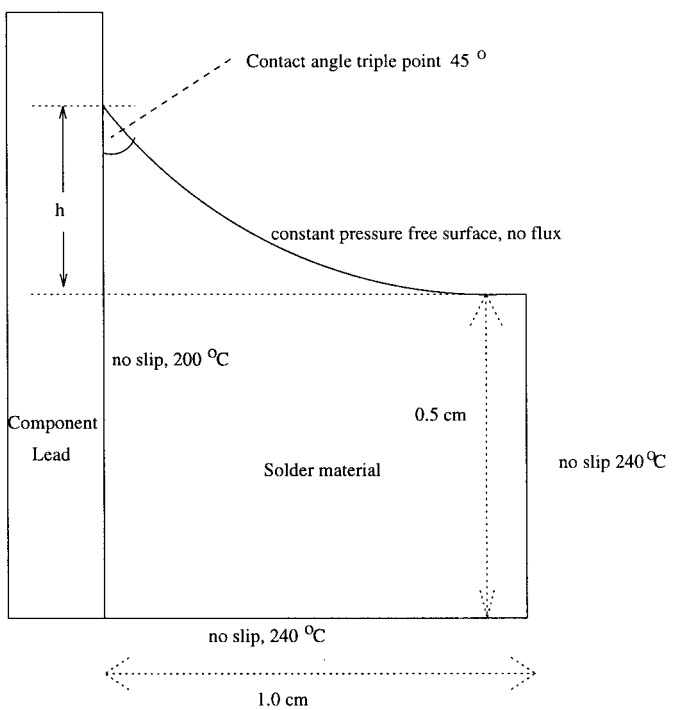

Figure 16. Wetting balance boundary conditions.

Table I. Material properties for solder and oil.

Material property	Oil	Solder	Unit
g	10	10	$m\,s^{-2}$
γ	0.0208	0.4	$J\,m^{-2}$
ρ	963.0	8000	$kg\,m^{-3}$
μ	0.048	0.0022	$kg\,m^{-1}\,s^{-1}$
α	−0.000065	−0.000053	$J\,m^{-2}\,K$
β	−0.9	−0.12	$kg\,m^{-3}\,K$
k	14.0E+01	5.0E+01	$kg\,m\,s^{-3}\,K$
c	20.0E+02	1.5E+02	$m^2\,s^{-2}\,K$

the Marangoni number given by

$$Ma = \frac{\rho_0 \alpha H \Delta T c}{\mu k} \tag{34}$$

the Capillary number given by

$$Ca = \frac{\alpha \Delta T}{\gamma_0} \tag{35}$$

the Rayleigh number given by

$$Ra = \frac{H^3 \rho_0^2 c \beta \Delta T g}{k \mu} \tag{36}$$

the Prandtl number given by

$$Pr = \frac{\mu c}{k} \tag{37}$$

and, lastly, the dynamic bond number given by

$$Bo_d = \frac{Ra}{Ma} \tag{38}$$

In these expressions, H is the height of the cavity, g is the acceleration due to gravity, γ_0 is the reference surface tension, ρ_0 is the reference density, α is the rate of change of surface tension with temperature, ΔT is the change in temperature over the domain and β is the thermal expansion coefficient. Ma and Ra were chosen to depend on the viscous time scales and the thermal time scales [25]. Surface tension is given by

$$\gamma = \gamma_0 + \alpha(T - T_0) \tag{39}$$

and the density for the Boussinesq approximation is given by

$$\rho = \rho_0 + \rho_0 \beta (T - T_0) \tag{40}$$

The values of the dimensionless parameters are given in Table II. The value of Bo_d is greater than unity in both cases indicating that buoyancy forces are important. Ca is small for solder indicating that the surface will be governed more by surface tension forces and less affected by Marangoni convection. Bo is large in both cases, indicating that the gravitational field will dominate the surface shape.

The first simulations show model predications when convection is neglected. These are compared with elastica calculations and validate mesh movement. The equilibrium position when no conversion is presented is given from static theory, and is used to validate the steady state surface position. Meshes of 11×5, 21×10 and 41×20 elements are employed. The difference between the static equilibrium and the numerical steady state solution is given as a percentage error in Figures 17 and 18. For both oil and solder the error is less than 2 per cent for the finest mesh and the error decreases as the mesh is refined.

When residual convection is present a change in the equilibrium free surface position can be seen (Figures 19 and 20). In oil at 100°C the triple point rises when Marangoni convection is included but falls for buoyancy convection (Table III). In Figure 21 the flow regimes and the temperature contours can be seen for Marangoni and buoyancy convection. The velocity magnitudes are considerably lower for buoyancy induced flow as opposed to Marangoni induced flow. The Marangoni induced flow creates a larger temperature gradient near the triple point then the buoyancy induced flow (Figure 21). In the case of buoyancy flow, the

Table II. Dimensionless parameters.

Parameter	Oil	Solder
Bo	11.57	5
Ca	6.98	115.64
Ra	23.29	529.53
Pr	0.69	0.006
Bo_d	3.34	4.58

Table III. Height rise for oil at 100°C.

Oil 100°C	Simulation	Experiment
θ	45.0	3.4
dT/dx	7.5	
Static (elastica value)	0.958	1.90
Marangoni	1.280	
Buoyancy	0.885	
Buoyancy and Marangoni	1.019	
Experimental		2.5
Per cent rise (Marangoni)	34	32

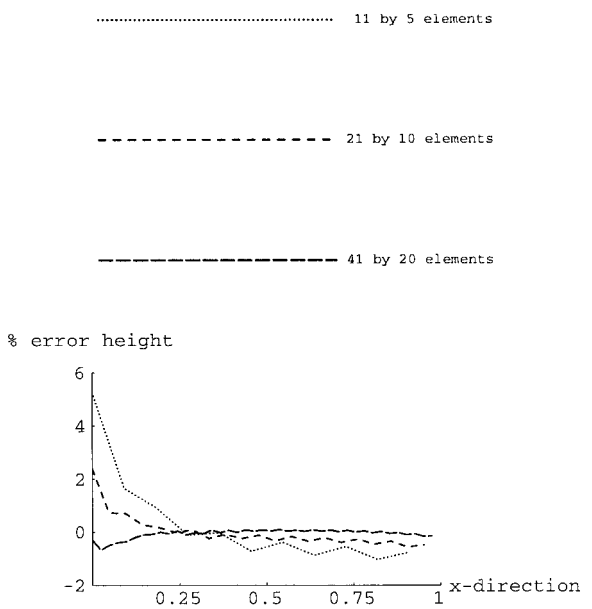

Figure 17. Per cent error in static free surface position for oil.

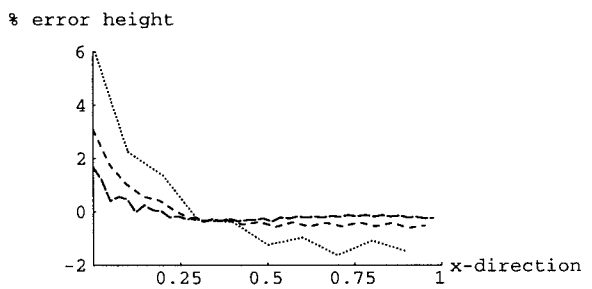

Figure 18. Per cent error in static free surface position for solder.

dependence of surface tension on temperature has been removed, so the surface tension takes a fixed value. This may cause differences between the Marangoni induced and the buoyancy induced flow free surface profiles. The surface tension decreases away from the triple point in the case of Marangoni flow due to a negative dependence on temperature, which causes a height rise. A recirculation is occurring for buoyancy induced flow near the triple point, which may also effect the height. The static height in the experimental column of Tables III, IV and V is computed using the experimental value of the contact angle and force using the elastica solution. In all cases it does not agree with the experimental height prediction. Experimental

results in Table III agree with the Marangoni convection but not with the combined buoyancy–Marangoni convection. The 32 per cent height rise for the experiment agrees well with the 34 per cent height rise for the simulation. Thus, the buoyancy effects may be overstated in these simulations or another physical process may be influencing the experiment. In oil at 50°C, the same effect is found for Marangoni convection agreeing with experiment results by Moon *et al.* (Table IV).

For solder, the interface change can be seen in Figure 20. Combined buoyancy–Marangoni convection gives the largest height rise. Marangoni and buoyancy driven convection also result in height rises. The low value of *Ca* allows relatively small movement of the surface for solder

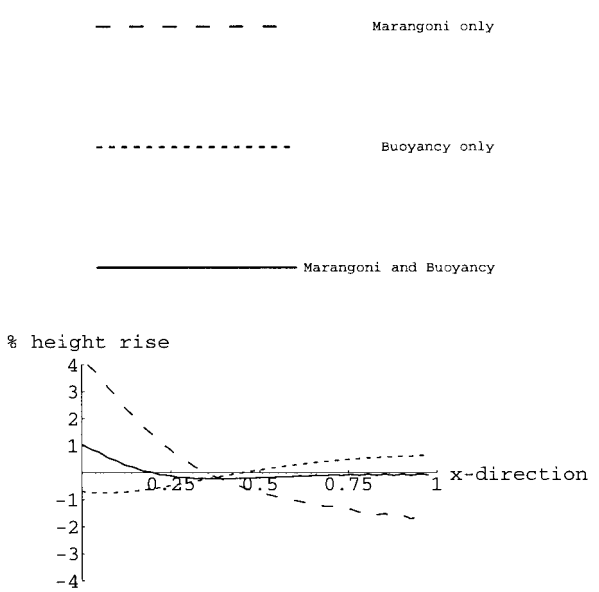

Figure 19. Per cent change in the free surface height caused by different flow regimes in oil.

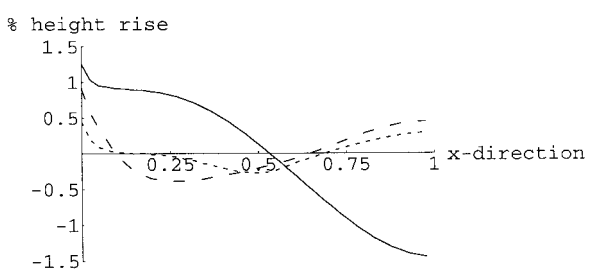

Figure 20. Per cent change in the free surface height caused by different flow regimes in solder.

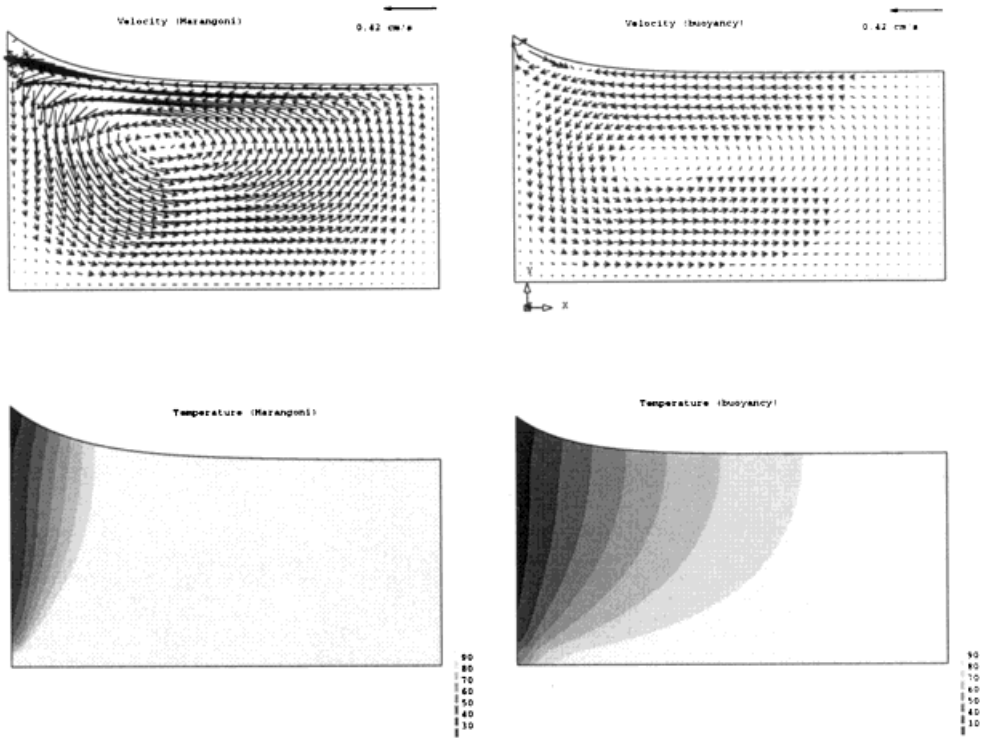

Figure 21. Various steady flow regimes for oil.

compared with oil. The flow pattern has less influence on the temperature field owing to a lower value of *Pr*. The 10 and 15 per cent height rise for the simulation and experiment respectively in Table V, agree well, indicating that buoyancy–Marangoni combined convection may explain the results found in the experiment.

4.4. Case 4: simulation of the wetting balance test in three dimensions

To test the three-dimensional implementations of this method, the wetting balance is again modelled. A simulation in three dimensions was attempted to validate the static free surface position and the trends due to Marangoni convection. Equation (29) was used to improve the stability allowing larger time steps. Figure 22(a) shows a comparison of the displacement of the contact point with time, for relaxation of $\alpha = 0.5$ and $\alpha = 0.0$. The dynamics are only effected by a small amount when the relaxation is present, thus $\alpha = 0.5$ for this simulation. The wetting balance simulation presented here is for a rectangular pin in a circuit oil bath. The radius of the bath is 5 cm and the depth is 5 cm. The square pin measures $10 \times 5\,\text{mm}^2$. The static

Table IV. Height rise for oil at 50°C.

Oil 50°C	Simulation	Experiment
θ	40.1	21.9
dT/dx	17.5	
Static (elastica value)	1.043	1.72
Marangoni	1.381	
Buoyancy		
Buoyancy and Marangoni		
Experimental		1.92
Per cent rise (Marangoni)	32	12

Table V. Height rise of solder.

Solder	Simulation	Experiment
θ	45.0	41
dT/dx	4.0	
Static	6.202 (1.482)	1.55
Marangoni	6.258 (1.520)	
Buoyancy	6.229 (1.498)	
Buoyancy and Marangoni	6.280 (1.627)	
Experimental		1.79
Per cent rise (B–M)	10	15

equilibrium shape is compared with the SE prediction in Figure 22(b) for mesh densities of 15, 29 and 49 elements along the free surface. The mesh density is course in these simulations due to the time step limit an explicit scheme imposes. Errors of less than 2 per cent are achieved for all three mesh densities. Wedge elements were used throughout the mesh, which can be seen in Figure 23. The temperature field, resultant velocity field and velocity cross-section can be seen in Figures 24–26 respectively. This simulation demonstrates the ability of this method to simulate three-dimensional surface tension problems using unstructured meshes. The free surface shape compares well with Surface Evolver predictions.

5. CONCLUSION

The surface tension boundary condition has been implemented in a finite volume framework using a novel approach on three-dimensional unstructured meshes. The numerical method has been tested against several closed form solutions for Maragoni flow. A fixed-Lagrangian approach with a kinematic update has been used to capture the deformation of the free surface. The resulting steady state solutions compare well with the elastic solution. Finally, the method has been used to provide insight into the wetting balance test, predicting how natural and Marangoni convection affect the free surface. It was found that Marangoni convection predicted the correct height rise in the case of oil, but including buoyancy flow resulted in a

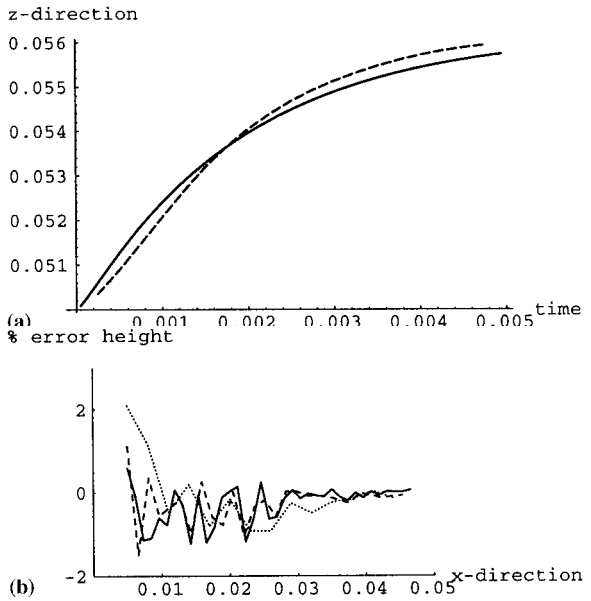

Figure 22. (a) Contact point displacements for (1) $\alpha = 0.5$ (dashed), and (2) $\alpha = 0.0$ (solid). (b) Per cent error in the static equilibrium free surface height for 15, 29 and 49 elements.

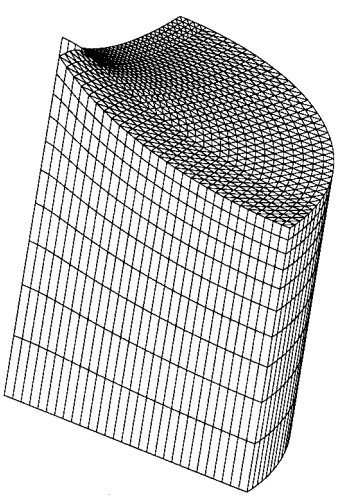

Figure 23. Mesh used for the simulation showing final deformation.

decrease in the height of the triple point. This indicates that the temperature assumed in this analysis is possibly too large. For the case of solder, the combined buoyancy–Marangoni convection showed an increase in the height. This may explain the height rise found in the experiments. Furthermore, three-dimensional predictions were validated against static Surface Evolver predictions, and Marangoni convection also showed a height increase in the case of oil.

Instability in mesh movement required small time steps for the materials considered here and numerical damping in the case of solder. Improvements have been made by using the previous time step displacement combined with the current time step displacement. This acts to dampen any instability while preserving the dynamics of the system. Using this method time steps of an order of magnitude greater were used, saving on run times. A fully implicit boundary condition needs to be developed for the finite volume framework and will form the basis of further work. This may overcome some of the stability problems encountered here.

With regard to the modelling of complex industrial processes, predicting surface tension phenomena is extremely useful when coupled with other physical behaviour, such as phase change, associated heat transfer, and solid mechanics. This can be achieved within the numerical framework PHYSICA. Further work will include simulations for solder wetting with solidification and implementation of an implicit formulation for the surface tension boundary condition.

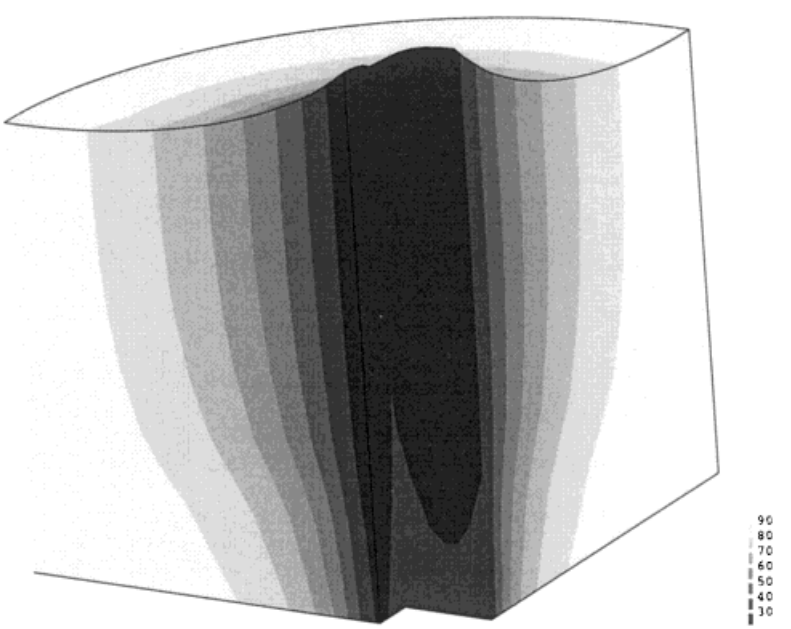

Figure 24. Temperature field in the oil.

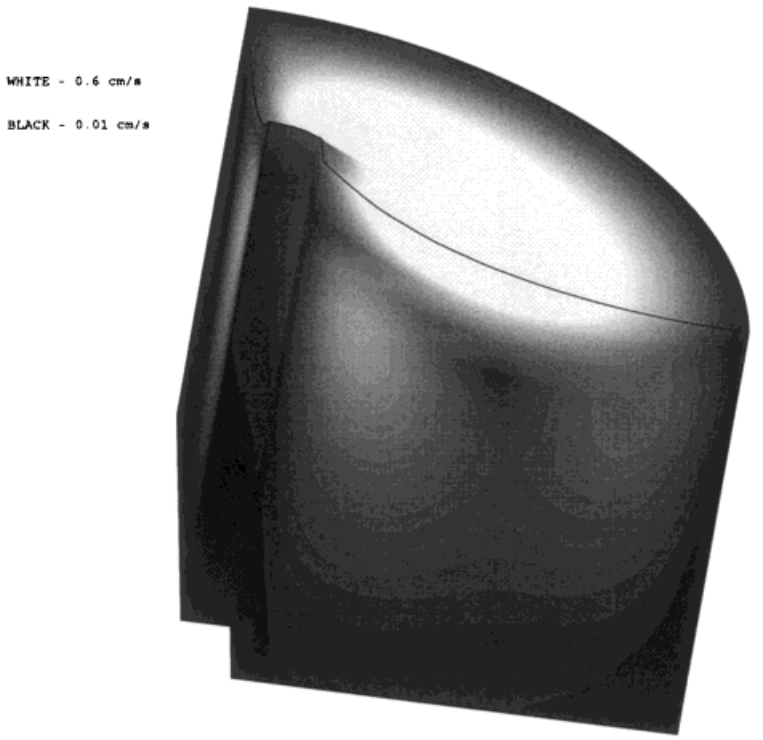

Figure 25. Velocity magnitude in the oil.

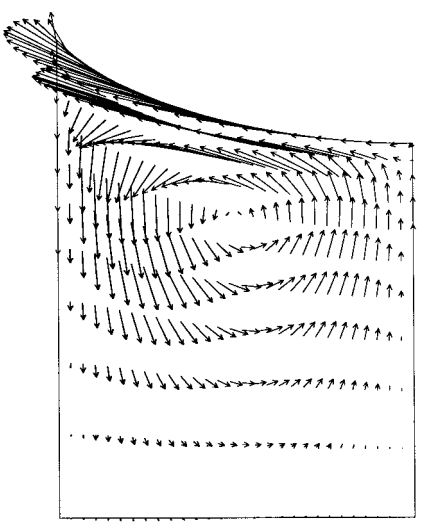

Figure 26. Cross-section through domain showing velocity vectors due to Marangoni flow.

ACKNOWLEDGMENTS

The authors would like to acknowledge the financial support of the University of Greenwich and the National Institute of Standard and Technology.

REFERENCES

1. Ahmed I, Ball KS. Special simulation of thermocapillary convection with deformable free surface. *Numerical Heat Transfer* 1997; **32**: 127–149.
2. Sasmal GP, Hochstein JI. Marangoni convection with a curved and deforming free surface in a cavity. *Journal of Fluid Engineering* 1994; **116**: 577–582.
3. McClelland MA. Time-dependent liquid metal flows with free convection and a deformable free surface. *International Journal for Numerical Methods in Fluids* 1995; **20**: 603–620.
4. Slikkerveer PJ, Van Lohuizen EP, O'Brien SBG. An implicit surface tension algorithm for picard solvers of surface-tension dominated free and moving boundary problems. *International Journal for Numerical Methods in Fluids* 1996; **22**: 851–865.
5. Racz LM, Szekely J, Brakke KA. Determination of equilibrium shapes and optimal volume of solder droplets in the assembly of surface mounted integrated circuits. *ISIJ International* 1993; **33**: 336–342.
6. Brakke KA. SURFACE EVOLVER. The Geometry Centre 1300 South Second Street, Minneapolis MN 55454, 2.00 Edition, April 1996 (available from http//ww/geom.umn.edu).
7. Whalley DC, Conway PP. Simulation and interpretation of wetting balance tests using the SURFACE EVOLVER. *Transactions of the ASME* 1996; **118**: 134–141.
8. Wheeler D, Bailey C, Cross M. A computational modelling framework to predict macroscopic phenomena in solder joint formation. *Proceedings of the Institute of Mechanical Engineers* 1998; **212**: 141–157.
9. Wu X, Li F, Tang KH, Yeh C, Wyatt K. Solder joint design optimization for fine pitch component applications. Inter Society Conference on Thermal Phenomena, 1996; 236–240.
10. Moon KW, Boettinger WJ, Williams ME, Josell D, Murray BT, Carter WC, Handwerker CA. Dynamic aspects of wetting balance tests. *Transactions of the ASME* 1996; **118**: 174–183.
11. Patankar SV. *Numerical Heat Transfer and Fluid Flow*. Hemisphere: New York, 1980.
12. Croft TN. Unstructured mesh-finite volume algorithms for swirling, turbulent, reacting flows. PhD thesis, University of Greenwich, 1993.
13. Versteeg HK, Malaseekera W. *An introduction to Computational Fluid Dynamics*, *The Finite Volume Method*. Longman Scientific & Technical: Harlow, 1995.
14. Sarpkaya T. Vorticity free surface and surfactants. *Annual Review of Fluid Mechanics* 1996; **23**: 83–128.
15. Singler TJ, Zhang X. A computational study of non-isothermal spreading of drops on a horizontal surface. *Advances In Electronic Packaging ASME* 1997; **19**: 1383–1389.
16. Weatherburn CE. *Differential Geometry in Three Dimensions*. Cambridge University Press: Cambridge, 1972.
17. University of Greenwich, Wellington Street, London SE18 6PF, U.K. PHYSICA—A software environment for the modelling of multi-physics phenomena (available from http://physica.gre.ac.uk/) 1999.
18. Bailey C, Chow P, Cross M, Pericleous K. Multi-physics modelling of the metal casting process. *Proceedings of the Royal Society of London A* 1996; **452**: 459–486.
19. Cross M. Computational issue in the modelling of materials based manufacturing processes. *Journal of Computer Aided Design* 1996; **3**: 100–116.
20. Chow P. Control volume unstructured mesh procedure for convection–diffusion solidification processes. PhD thesis, University of Greenwich, 1993.
21. Taylor G. A vertex based discretization scheme applied to material non-linearity within a multi-physics finite volume framework. PhD thesis, University of Greenwich, 1996.
22. Slone AK, Pericleous K, Bailey C, Cross M. Dynamic fluid–structure interacting using finite volume unstructured mesh procedures. *International Forum on Aeroelasticity of Structured Dynamics* 1997; **2**: 417–424.
23. Gupaloa P, Ryazantsev S. Thermocapillary motion of a liquid with a free surface with non-linear dependence of the surface tension on the temperature. *Izvestiya Akademii Nauk SSSR* 1988; **5**: 132–137.
24. Erhad P, Davis SH. Non-isothermal spreading of liquid drops on horizontal plates. *Journal of Fluid Mechanics* 1991; **229**: 365–388.
25. Thess A, Orzag SA. Surface-tension driven Benard convection at infinite Prandtl number. *Journal of Fluid Mechanics* 1995; **283**: 201–230.

